Partial Differential Equations in Applied Mathematics 10 (2024) 100704

Contents lists available at ScienceDirect

Partial Differential Equations in Applied Mathematics

journal homepage: www.elsevier.com/locate/padiff

The analytical solutions of squeezing flow and heat transfer in an horizontal filtering channel

Thabo Joseph Itumeleng [a,*], Gabriel Magalakwe [b], Modisawatsona Lucas Lekoko [a], Letlhogonolo Daddy Moleleki [a]

[a] School of Mathematical and Statistical Sciences, North-West University, Mafikeng Campus, Private Bag X2046, Mmabatho 2735, South Africa
[b] School of Mathematical and Statistical Sciences, North-West University, Potchefstroom Campus, Private Bag X6001, Potchefstroom 2520, South Africa

ARTICLE INFO

Keywords:
Magnetohydrodynamics
Squeezing flow
Horizontal
Filtration process
Lie group method
Perturbation approximation

ABSTRACT

Flow and heat transfer dynamics inside different industrial chambers play a vital role in understanding momentum and heat transfer during industrial operations. Analysis of such flow and heat transfer helps operators to know how the system works. To better understand the filtration process, the current study analytically investigated the internal flow and heat transfer through a porous horizontal filter channel under the influence of a uniform magnetic field while removing unwanted contaminations from the fluid inside the filter chamber. Thus, the novelty of the current study is to advance the filtration process by investigating how the top moving wall, which aims to minimise filter cake formation, affects permeates outflow (the current design). The partial differential equations (PDEs) model representing the internal flow and heat transfer during filtration is transformed into a system of ordinary differential equations (ODEs) using Lie point symmetry reduction without changing the dynamics under investigation. After that, the transformed equations are solved analytically using the perturbation approximation technique. The comparative analysis between the obtained semi-analytical and NDSolve numerical solutions was used to show the correlation of internal flow, temperature, and pressure profiles. The obtained solutions are used to find the best combination of dimensionless parameters that arise from flow and heat transfer dynamics that lead to optimum outflow. Graphical analysis of flow and heat transfer dynamics are used to indicate the combination of parameters that leads to maximum outflow based on scientific evidence. It is observed that, on average, the velocity increases significantly by 122.55% across all cases of R_e ranging from 0 to 3.2 at the top permeable wall $y = 1$. This significant increase is due to the motion of the moving wall and fluid injection happening at $y = 1$. The results show that more chamber volume, small pores size, weak injection, weak magnetic force, and less Joule heating are crucial to increase internal temperature and permeate outflow velocity during filtration.

1. Introduction

It is crucial to consider several important factors when processing liquid for human consumption or industrial purposes. The effectiveness of the filtration method used to reduce/remove deposited particles in a liquid depends mainly on the type of particles, the quality of the filter media, and the design of the filter. This important process of filtering contaminants from the fluid is one process that scientists and engineers must understand to fully implement filtering processes that meet a particular standard requirement to achieve various clean industrial fluids. Such processes can be understood through research works, such as theoretical analysis and experiments, to name a few. To comprehend the experimental findings, designers and engineers need a theoretical foundation (model) to construct practical and optimal filtering designs. From the correlation of experiments and model analysis, designers get an idea and better grasp of how the system works. Thus, such models and experiments are important solutions to the industry.

Driven by the quest to understand various flow and heat transfers between parallel plates and their applications in the compression process, fluid purification, polymer process, transportation inside living bodies, filtration, and flow inside syringes. There has been a rise in considering these flows for research interest, and numerous scientific studies have focused their efforts on understanding such flows. The work of Thorpe[1] conducted the squeezing of a film of liquid bounded by two parallel surfaces. Siddiqui et al.[2] disclosed an analytical procedure for solving equations describing the squeezing flow between two

* Corresponding author.
E-mail addresses: 23995394@nwu.ac.za (T.J. Itumeleng), Gabriel.Magalakwe@nwu.ac.za (G. Magalakwe), lucaslekoko@nwu.ac.za (M.L. Lekoko), Letlhogonolo.Moleleki@nwu.ac.za (L.D. Moleleki).

https://doi.org/10.1016/j.padiff.2024.100704
Received 28 December 2023; Received in revised form 6 April 2024; Accepted 2 May 2024
Available online 7 May 2024

NOMENCLATURE

t	time (s)
T	temperature (K)
$\bar{x}$	axial coordinate (m)
$\bar{y}$	normal coordinate (m)
$\bar{u}$	axial velocity (m/s)
$\bar{v}$	normal velocity (m/s)
$\bar{P}$	internal pressure (Pa)
q_r	radiative heat flux (W/m^2)
g	gravitational acceleration (m/s^2)
U_w	velocity at wall (m/s)
k	permeability (H/m)
c_p	heat capacitance (J/(kgK))
B_0	magnetic field strength (A/m)

Greek symbols

ν	kinematic viscosity (m^2/s)
σ	electrical conductivity (S/m)
ϕ	porosity parameter (cm^2/s)
ρ	fluid density (kg/m^3)
β	thermal expansion $(1/K)$

Non-dimensional variables

$\bar{t}$	non-dimensional time
x	non-dimensional axial coordinate
y	non-dimensional normal coordinate
u	non-dimensional axial velocity
v	non-dimensional normal velocity
P	non-dimensional internal pressure
R_e	Reynolds permeation number
G_r	Grashof number
N	Stuart number
P_r	Prandtl number
J	Joule heating parameter
R	radiation parameter
K	permeation parameter
α	wall dilation rate
C_f	skin friction coefficient
N_u	Nusselt number

Subscripts

w	wall condition
h	filter height

parallel plates. The authors noted that the method gives freedom of selecting the homotopy parameter R, and it is not limited to R being small, unlike in the case of the perturbation method. A similar study by Domairy and Aziz[3] was investigated between two infinite disks with one porous disk to allow fluid injection/suction while the other disk was impermeable.

Rashidi et al.[4] investigated the unsteady squeeze of a viscous fluid between two parallel plates. Similarity transformations were used to reduce the Navier–Stokes equations to fourth-order nonlinear ODEs, and after that, solutions were found using the Homotopy Analysis Method. Various researchers have concentrated their efforts towards finding solutions of such flows of industrial importance in different geometries, such as the works of Refs. 5–10 to name a few. Most industrial fluids are electrically conducting and possess a presence of electromagnetic or magnetic field, which can change the flow dynamics. Hence, it is important to study flow under the effect of magnetic strength to observe how magnets influence the flow dynamics. The squeeze flow in various designs under the influence of magnetic force has been investigated in Refs. 11–13 by researchers. Khan et al.[14] modelled the equations of flow behaviour between two squeezing plates in the presence of magnetic strength. The authors used the parametric continuation method to solve the flow equation. They found that swelling of the magnetic strength enhances the temperature. The squeezing magnetohydrodynamic flow was investigated over a permeable stretching surface in the presence of nanoparticles by Hayat et al.[15] The authors found that strengthening the magnetic parameter decreases the velocity profiles for the suction case.

Since most squeezing flows of industrial importance experience temperature variation, much research has been done to understand the impact of heat transfer within such flow dynamics. To gain a better understanding of the behaves of squeeze flow and heat transfer, the solutions of such flows can be obtained using numerical simulations such as the works of Salehi et al.[16] or analytical procedures used in the study by Rahimi-Gorji et al.[17] The works of Abbas et al.[18] have investigated the effects of heat transfer in hybrid nanofluid flow over a nonlinear curved stretching surface. A similar study has been done, such as the works of Gumber et al.,[19] in which the heat transfer in micropolar hybrid nanofluid flow past a vertical plate in the presence of thermal radiation and suction/injection effects have been investigated.

The use of the Homotopy perturbation method to investigate various flow and heat transfer systems was done by Akinshilo.[20–22] In the paper,[20] the author studied heat and mass transfer of Prandtl nanofluid flow over a vertically heated curved surface to investigate the effects of the magnetohydrodynamics (MHD), thermal radiation, and chemical reactions on the system. The author also studied a magnetohydrodynamic nanofluid's flow and heat transfer characteristics with internal heat generation in a rotating system.[21]. Lastly, in, Ref. 22 the author focused on a non-Newtonian third-grade fluid's flow and heat transfer characteristics between parallel plates held horizontally layered with a porous medium under the influence of an internal heat source. A different perturbation technique called the homotopic analysis method was used to study flow and heat transfer by Rasheed and co-authors.[23–25] The joint work of Rasheed et al.[23] investigated the impact of heat transfer in various applications, focusing on utilising non-Newtonian fluids in biological and engineering disciplines. Rasheed et al.[24] studied the unsteady magnetohydrodynamic (MHD) mixed convective and thermally radiative behaviour of Jeffrey nanofluid flow around a vertical stretchable cylinder. Recently, Haroon et al.[25] investigated the thermal characteristics and mass transfer in a non-Newtonian fluid system. They focused on viscoelastic nanofluid flow driven by a permeable stretchable surface.

Reducing the complex mathematical model that describes the squeeze flow and heat transfer dynamics to a solvable model became a prominent part of research over the years. Researchers in Refs. 26–30 used different methods to find similarity transformation to reduce partial differential equations to ordinary differential equations. For those models where the similarity solutions cannot be found easily using the usual similarity transformations method, Sophus Lie discovered a mathematical tool called Lie group analysis to cater for such problems. The group invariant similarity transformation can be utilised as an impressive tool to solve initial BVP (Boundary Value Problems) see Refs. 31–34. This method gives various similarity transformations which map the PDEs under investigation into simpler and solvable ODEs.

During the filtration process, forming a filter cake is one challenge when permeable surfaces effectively restrict particles from entering the filter chamber. The current study seeks to deal with this formation of filter cake during the filtration process by studying a flow and heat transfer inside the filter chamber that allows the top wall to move in the axial direction to minimise the formation of the filter cake. Thus, for the first time, the current study advances the filtration process by

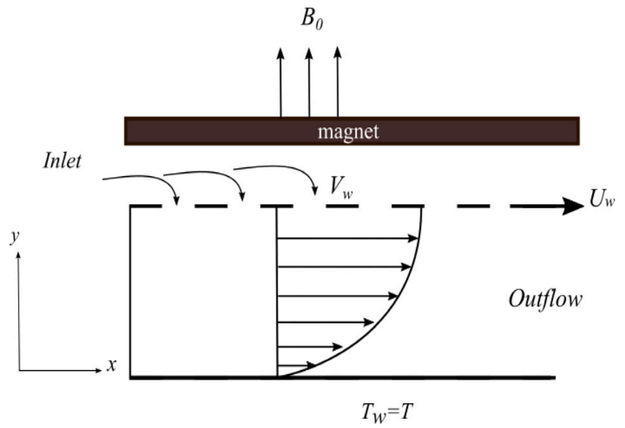

Fig. 1. Geometry of the flow.

investigating horizontal flow behaviour which arises from moving the top wall (the current design). The current case study aims to analyse the effects of thermal physical parameters that arise from the current filter chamber and the inclusion of heat effects on the system, such as Prandtl number, radiation and Joule heating on permeate outflow.

2. Theoretical model

We consider a two-dimensional flow model of a viscous magnetohydrodynamic fluid in a horizontal squeezing (expanding or contracting) filter channel with a porous upper plate moving with constant speed U_w to minimise filter cake formation. The flow is two-dimensional since the current design is such that the work done by the chamber walls in the z-direction does not yield any momentum variation. The lower plate is fixed and impermeable while kept at a constant temperature T_w to decrease viscous effects at the bottom of the filter chamber. Also, the normal velocity remains unchanged as the flow approaches the lower plate, i.e. $v_y = 0$ at $y = 0$. Pressure p_w due to work done by the lower plate affects the system such that the pressure towards the upper is either minimum or maximum. The fluid flow inside the filter chamber is due to constant fluid injection velocity V_w, perpendicular to the upper plate, the plate movement and pressure difference due to the filter chamber being closed on the left and open on the right to allow outflow as shown in Fig. 1. Thus the two-dimensional flow of a viscous magnetohydrodynamic fluid and heat transfer inside a filter chamber is mathematically represented as follows[31]

$$\partial_{\bar{x}}\bar{u} + \partial_{\bar{y}}\bar{v} = 0, \tag{1}$$

$$\partial_t\bar{u} + \bar{u}\partial_{\bar{x}}\bar{u} + \bar{v}\partial_{\bar{y}}\bar{u} + \rho^{-1}\partial_{\bar{x}}\bar{p} - \nu\left[\partial_{\bar{x}\bar{x}}\bar{u} + \partial_{\bar{y}\bar{y}}\bar{u}\right] + \frac{\nu\phi}{k}\bar{u} + \frac{\sigma B_0^2}{\rho}\bar{u} = 0, \tag{2}$$

$$\partial_t\bar{v} + \bar{u}\partial_{\bar{x}}\bar{v} + \bar{v}\partial_{\bar{y}}\bar{v} + \rho^{-1}\partial_{\bar{y}}\bar{p} - \nu\left[\partial_{\bar{x}\bar{x}}\bar{v} + \partial_{\bar{y}\bar{y}}\bar{v}\right] + \frac{\nu\phi}{k}\bar{v} - g\beta(T - T_h) = 0, \tag{3}$$

$$\partial_t T + \bar{u}\partial_{\bar{x}}T + \bar{v}\partial_{\bar{y}}T - \frac{\bar{k}}{\rho c_p}\left[\partial_{\bar{x}\bar{x}}T + \partial_{\bar{y}\bar{y}}T\right] - \frac{1}{\rho c_p}\partial_{\bar{y}}q_r - \frac{\sigma B_0^2}{\rho c_p}\bar{u}^2 = 0, \tag{4}$$

subject to the following constraints

$$\begin{aligned}
&\text{(i)} && \partial_{\bar{y}}\bar{u}(\bar{x},1,t) = U_w, \quad \bar{v}(\bar{x},1,t) = -V_w, \quad \partial_{\bar{y}}\bar{p}(\bar{x},1,t) = 0, \quad \partial_{\bar{y}}T(\bar{x},1,t) = 0,\\
&\text{(ii)} && \bar{u}(\bar{x},0,t) = 0, \quad \bar{v}_{\bar{y}}(\bar{x},0,t) = 0, \quad \bar{p}(\bar{x},0,t) = \bar{p}_w, \quad T(\bar{x},0,t) = T_w,\\
&\text{(iii)} && \bar{u} = 0 \quad \text{at } \bar{x} = 0.
\end{aligned} \tag{5}$$

For radiative heat flux q_r, we consider the Rosseland approximation for optically thick medium defined in Refs. 35, 36 as

$$q_r = -\frac{4}{3k_*}\nabla e_b, \tag{6}$$

where the Stefan–Boltzmann radiative law allows us to define e_b to be $e_b = \sigma_* T^4$. Thus, nonlinear radiation[35,36] is defined mathematically as

$$q_r = \frac{-4\sigma^*}{3k^*}\partial_y T^4 = -\frac{4\sigma^*}{3k_r}\partial_y\left[4T_h^3 T - 3T_h^4\right], \tag{7}$$

where $T^4 \cong 4T_h^3 T - 3T_h^4$ is represented as a linear combination of temperatures using series expansion around T_h.

Using the radiative heat flux (7) and invoking the following dimensionless relations[31]

$$\begin{aligned}
&u = \frac{\bar{u}}{V_w}, \quad v = \frac{\bar{u}}{V_w}, \quad x = \frac{\bar{x}}{h(t)}, \quad y = \frac{\bar{y}}{h(t)}, \quad p = \frac{\bar{p}}{\rho V_w^2},\\
&t = \frac{\bar{t}V_w}{h}, \quad \alpha = \frac{h\dot{h}}{\nu}, \quad \theta = \frac{T - T_h}{T_w - T_h}, \quad V_w = \frac{\nu}{h},
\end{aligned} \tag{8}$$

we get the transformed form of Eqs. (1)–(4) and boundary conditions (5) in dimensionless form as

$$\partial_x u + \partial_y v = 0, \tag{9}$$

$$\partial_t u + u\partial_x u + v\partial_y u + \partial_x p - R_e{}^{-1}\left[\alpha y\partial_y u + \partial_x^2 u + \partial_y^2 u\right] + K^{-1}u + Nu = 0, \tag{10}$$

$$\partial_t v + u\partial_x v + v\partial_y v + \partial_y p - R_e{}^{-1}\left[\alpha y\partial_y v + \partial_x^2 v + \partial_y^2 v\right] + K^{-1}v - G_r\theta = 0, \tag{11}$$

$$\partial_t\theta + u\partial_x\theta + v\partial_y\theta - P_r^{-1}R_e^{-1}\left[\partial_x^2\theta + (1 - 4R)\partial_y^2\theta\right] - Ju^2 = 0, \tag{12}$$

where $R_e = \frac{hV_w}{\nu}$, $K = \frac{kV_w}{\nu h\phi}$, $N = \frac{\sigma h B_0^2}{\rho V_w}$, $G_r = \frac{hg\beta(T_w - T_h)}{\nu^2}$, $P_r = \frac{\rho C_p \nu}{k}$, $J = \frac{\sigma B_0^2 h V_w}{\rho C_p(T_w - T_h)}$, and $R = \frac{4\sigma_r T_h^3}{3k_r k}$. The boundary conditions take the following form

$$\begin{aligned}
&\text{(i)} && \partial_y u(x,1,t) = 1, \quad v(x,1,t) = -1, \quad p_y(x,1,t) = 0, \quad \partial_y\theta(x,1,t) = 0,\\
&\text{(ii)} && u(x,0,t) = 0, \quad v_y(x,0,t) = 0, \quad p(x,0,t) = 1, \quad \theta(x,0,t) = 1,\\
&\text{(iii)} && u = 0 \quad \text{at } x = 0.
\end{aligned} \tag{13}$$

For the steady-state operation of the filter chamber, the above system of equations and its boundary conditions reduce to

$$\partial_x u + \partial_y v = 0, \tag{14}$$

$$u\partial_x u + v\partial_y u + \partial_x p - R_e{}^{-1}\left[\alpha y\partial_y u + \partial_x^2 u + \partial_y^2 u\right] + K^{-1}u + Nu = 0, \tag{15}$$

$$u\partial_x v + v\partial_y v + \partial_y p - R_e{}^{-1}\left[\alpha y\partial_y v + \partial_x^2 v + \partial_y^2 v\right] + K^{-1}v - G_r\theta = 0, \tag{16}$$

$$u\partial_x\theta + v\partial_y\theta - P_r^{-1}R_e^{-1}\left[\partial_x^2\theta + (1 - 4R)\partial_y^2\theta\right] - Ju^2 = 0, \tag{17}$$

as well as the following boundary conditions

$$\begin{aligned}
&\text{(i)} && \partial_y u(x,1) = 1, \quad v(x,1) = -1, \quad p_y(x,1) = 0, \quad \partial_y\theta(x,1) = 0,\\
&\text{(ii)} && u(x,0) = 0, \quad v_y(x,0) = 0, \quad p(x,0) = 1, \quad \theta(x,0) = 1,\\
&\text{(iii)} && u = 0 \quad \text{at } x = 0.
\end{aligned} \tag{18}$$

According to the current design, the filter chamber is such that the upper wall (at $y = 1$) accelerates at and maintains constant acceleration while allowing fluid injection. Also, the wall does not allow heat to flow through. Due to the bottom stationary wall, the layers near the bottom wall approximate the velocity of the wall (no-slip condition). The bottom wall is maintained at a constant temperature and exerts a constant pressure.

3. Solution method

The Lie-point symmetries method[32,37,38] has now been introduced to reduce the dimensionless system of Eqs. (14)–(17) governing flow and heat transfer inside a filter channel to a system of ordinary differential equations.

3.1. Calculating Lie-point symmetries

The one-parameter Lie group of transformation for (14)–(17) and the corresponding vector field X is defined as follows[39]

$$
\begin{aligned}
x^* &= x + \varepsilon\xi_1(x, y, u, v, p, \theta) + 0(\varepsilon^2),\\
y^* &= y + \varepsilon\xi_2(x, y, u, v, p, \theta) + 0(\varepsilon^2),\\
u^* &= u + \varepsilon\eta_1(x, y, u, v, p, \theta) + 0(\varepsilon^2),\\
v^* &= v + \varepsilon\eta_2(x, y, u, v, p, \theta) + 0(\varepsilon^2),\\
p^* &= p + \varepsilon\eta_3(x, y, u, v, p, \theta) + 0(\varepsilon^2),\\
\theta^* &= \theta + \varepsilon\eta_4(x, y, u, v, p, \theta) + 0(\varepsilon^2),
\end{aligned}
\tag{19}
$$

and

$$
X = \xi_1\frac{\partial}{\partial x} + \xi_2\frac{\partial}{\partial y} + \eta_1\frac{\partial}{\partial u} + \eta_2\frac{\partial}{\partial v} + \eta_3\frac{\partial}{\partial p} + \eta_4\frac{\partial}{\partial \theta}, \tag{20}
$$

where $\xi_1, \xi_2, \eta_1, \eta_2, \eta_3$ and η_4 are infinitesimal transformation.

By carrying out the tedious algebra with the help of maple, we finally obtain that the non-linear system of Eqs. (14)–(17) admits the following three Lie-point symmetries:

$$
X_1 = \frac{\partial}{\partial x}, \quad X_2 = yG_r\frac{\partial}{\partial p} + \frac{\partial}{\partial \theta}, \quad X_3 = \frac{\partial}{\partial p}. \tag{21}
$$

For a more detailed procedure of finding symmetries of the system of equations, the reader is referred to the works of.[40]

The one-parameter group generated by the translation symmetries X_1 leaves the solutions $u = u(x, y)$, $v = v(x, y)$, $p = p(x, y)$ and $\theta = \theta(x, y)$ unchanged while reducing the number of independent variable, if

$$
\Phi_u = X(u - u(x, y)) = 0, \ \Phi_v = X(v - v(x, y)) = 0, \tag{22}
$$

$$
\Phi_p = X(p - p(x, y)) = 0, \ \Phi_\theta = X(\theta - \theta(x, y)) = 0 \tag{23}
$$

while the boundary conditions are not changed by this action.

3.2. Reduction

The steady-state regime of the case study is given by the translation symmetry X_1, which yields the following invariant surface condition solutions

$$
u = U(y), \quad v = V(y), \quad p = P(y), \quad \theta = \Theta(y), \tag{24}
$$

where the new variables U, V, P, and Θ represent axial and normal velocities, as well as pressure and temperature, respectively. It should be noted that the above invariants illustrate the dynamics of fully developed flow during the filtration process. Invoking (24) into the system of Eqs. (14)–(17) and boundary conditions (18) yields the following steady-state system

$$
V' = 0, \tag{25}
$$

$$
VU' - \frac{1}{R_e}\left[\alpha yU' + U''\right] + \frac{1}{K}U + NU = 0, \tag{26}
$$

$$
VV' + P' - \frac{1}{R_e}\left[\alpha yV' + V''\right] + \frac{1}{K}V - G_r\Theta = 0, \tag{27}
$$

$$
V\Theta' - \frac{(1-4R)}{P_rR_e}\Theta'' - JU^2 = 0, \tag{28}
$$

subject to the boundary conditions below

$$
\begin{aligned}
&\text{(i)} \qquad U'(1) = 1, \quad V(1) = -1, \quad P'(1) = 0, \quad \Theta'(1) = 0,\\
&\text{(ii)} \qquad U(0) = 0, \quad V'(0) = 0, \quad P(0) = 1, \quad \Theta(0) = 1,
\end{aligned}
\tag{29}
$$

where all the differentiations are executed with respect to y.

Solving (25) subject to boundary condition (29), gives

$$
V(y) = -1. \tag{30}
$$

The above results holds for $y > 0$.

With the findings above, the remaining equations from the system of ordinary differential Eqs. (25)–(28) become

$$
U'(y) + \frac{1}{R_e}\left[\alpha yU'(y) + U''(y)\right] - \frac{1}{K}U(y) - NU(y) = 0, \tag{31}
$$

$$
P'(y) - \frac{1}{K} - G_r\Theta(y) = 0, \tag{32}
$$

$$
-\Theta'(y) - \frac{(1-4R)}{P_rR_e}\Theta''(y) - JU^2(y) = 0, \tag{33}
$$

and the boundary conditions take the following form

$$
\begin{aligned}
&\text{(i)} \qquad U'(1) = 1, \quad P'(1) = 0, \quad \Theta'(1) = 0,\\
&\text{(ii)} \qquad U(0) = 0, \quad P(0) = 1, \quad \Theta(0) = 1.
\end{aligned}
\tag{34}
$$

3.3. Approximate analytical solutions

The perturbation method[31,41–43] is utilised in this subsection to obtain the approximate analytical solutions of the system of ordinary differential Eqs. (31)–(33) subject to the boundary conditions (34). The top moving wall is such that fluid permeation into the chamber is weak. Thus, the axial velocity solution U is represented in a series form in terms of weak permeation R_e as follows

$$
U = U_1 + R_eU_2 + R_e^2U_3 + O(R_e^3), \tag{35}
$$

where $U_i's$ are independent of the parameter R_e for $i = 1, 2, 3$. Substituting (35) into Eq. (31) and boundary conditions (34) generate the zeroth, first and second order equations of R_e together with appropriate boundary conditions below

$$
-\alpha yU_1'(y) - U_1''(y) = 0, \tag{36}
$$

$$
\frac{U_1(y)}{K} + NU_1(y) - \alpha yU_2'(y) + U_1'(y) - U_2''(y) = 0, \tag{37}
$$

$$
\frac{U_2(y)}{K} + NU_2(y) - \alpha yU_3'(y) + U_2'(y) - U_3''(y) = 0 \tag{38}
$$

as well as boundary conditions

$$
\text{(i)} \quad U_1'(1) = 1, \qquad \text{(ii)} \quad U_1(0) = 0, \tag{39}
$$

$$
\text{(iii)} \quad U_2'(1) = 0, \qquad \text{(iv)} \quad U_2(0) = 0, \tag{40}
$$

$$
\text{(v)} \quad U_3'(1) = 0, \qquad \text{(vi)} \quad U_3(0) = 0. \tag{41}
$$

Since the chamber walls dilate slowly and at a constant rate, the parameter α is utilised as a secondary perturbation parameter for velocity $U_1(y)$, $U_2(y)$ and $U_3(y)$ such that

$$
U_1(y) = U_{10}(y) + \alpha U_{11}(y) + \alpha^2U_{12}(y) + O(\alpha^3), \tag{42}
$$

$$
U_2(y) = U_{20}(y) + \alpha U_{21}(y) + \alpha^2U_{22}(y) + O(\alpha^3), \tag{43}
$$

and

$$
U_3(y) = U_{30}(y) + \alpha U_{31}(y) + \alpha^2U_{32}(y) + O(\alpha^3). \tag{44}
$$

Substituting the above equations into Eqs. (36), (37) and (38), as well as their corresponding boundary conditions, we obtain a set of equations by equating powers of the wall dilation rate (α). Solving those resulting equations, we obtain the axial velocity variation inside the filter chamber as

$$
\begin{aligned}
U(y) = \frac{1}{10080K^2}\Bigg[y\Bigg(&R_e^2\Big\{ -36\alpha\Big\{ A_4y^2(KN+1) + 105A_2Ky^5 - 105A_6Ky^3\\
&+ 420A_{11}Ky + 9A_2^2y^6 - 21A_5y^4 + A_3 \Big\} + \alpha^2\big(576A_2Ky^7 - 3780A_1Ky^5\\
&+ 1890A_6Ky^3 - 126A_{10}Ky + 43A_2^2y^8 - 36A_9y^6 + 126A_7y^4 - 84A_8y^2\\
&+ A_{12} + 14607 \big) + 1512\Big[K^2\Big(N^2\left(y^2-5\right)^2 + 10Ny(y-3)(y+1) + 80N\\
&+ 20[(y-3)y+3] \Big) + 2K\big(N\left(y^2-5\right)^2 + 5\left[y(y-3)(y+1)+8\right]\big) + \left(y^2-5\right)^2 \Big]\Big\}\\
&+3\ 6KR_e\Big\{ -42\alpha\left[-20A_1y^2 + A_{13} + 4y^4(KN+1) + 15Ky^3 - 30Ky\right]
\end{aligned}
$$

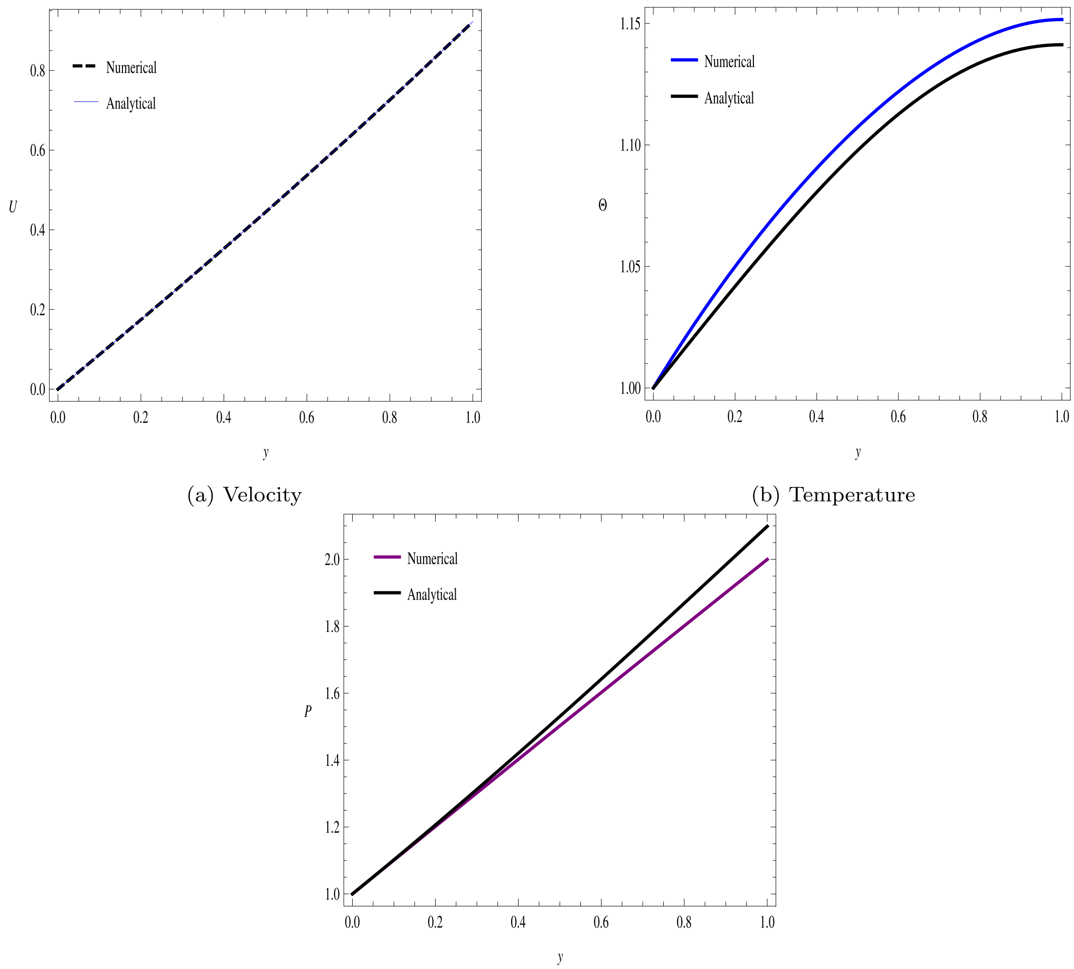

(a) Velocity (b) Temperature

(c) Pressure

Fig. 2. Comparison of semi-analytical and numerical profiles.

$$
\begin{aligned}
&+\alpha^2\left(23A_2y^6-21A_{14}y^4+35A_{15}y^2-7A_{10}+105Ky^5-315Ky^3+315Ky\right)\\
&+840\Big[K\big\{N\left(y^2-3\right)+3(y-2)\big\}+y^2-3\Big]\Big\}+1512K^2\Big[\alpha\Big\{15(\alpha+4)\\
&+3\alpha y^4-10(\alpha+2)y^2\Big\}+120\Big]\Big)\Big)\Big],
\end{aligned}
\tag{45}
$$

where A_i are constants defined in the Appendix. Similarly, the series solution of the temperature Θ is such that

$$\Theta(y)=\Theta+R_e\Theta+R_e^2\Theta+O(R_e^3). \tag{46}$$

Substituting the temperature series form (46) together with velocity (45) into the energy Eq. (33) and boundary conditions (34) yields a system of equations together with appropriate boundary conditions from equating zeroth, first and second order equations of R_e, which were rigorously solved to give the internal temperature variation below (see the work of Magalakwe et al.[39] for more details)

$$
\begin{aligned}
&\Theta(y)\\
&=\frac{1}{3632428800K(1-4R)^2}\Bigg[J(4R-1)yR_eP_r\Bigg(R_e\Bigg(17920\Big\{\alpha\Big[\alpha\{\alpha(957\alpha+7358)\\
&+29172\}+55341\Big]+54054\Big\}+K\Bigg(N\Bigg(17920\Big[\alpha\Big\{\Big(\alpha[\alpha(957\alpha+7358)+29172]\\
&+55341\Big\}+54054\Big]+4554\alpha^4y^{13}-91\alpha^3(671\alpha+964)y^{11}+4004\alpha^2[\alpha(99\alpha+284)\\
&+288]y^9-3003\alpha\Big(\alpha[\alpha(557\alpha+2320)+4320]+2640\Big)y^7+14014\Big\{\alpha\Big[\alpha\{\alpha(331\alpha\\
&+1832)+4800\}+5760\Big]+2880\Big\}y^5-105105[\alpha(\alpha+4)+8][\alpha(83\alpha+240)\\
&+360]y^3\Bigg)+21\Bigg(13\alpha^2[\alpha(49285\alpha+443036)+2037420]+480480(127\alpha+150)\\
&+1155\alpha^4y^{12}-1638\alpha^4y^{11}-10374\alpha^3(\alpha+2)y^{10}+16016\alpha^3(\alpha+2)y^9+5005\alpha^2\\
&[9\alpha(\alpha+4)+52]y^8-4290\alpha^2[19\alpha(\alpha+4)+112]y^7-107250\alpha(\alpha+2)[\alpha(\alpha\\
&+4)+8]y^6+240240\alpha(\alpha+2)[\alpha(\alpha+4)+8]y^5+135135[\alpha(\alpha+4)+8]^2y^4\\
&-450450[\alpha(\alpha+4)+8]^2y^3\Bigg)\Bigg)+4554\alpha^4y^{13}-91\alpha^3(671\alpha+964)y^{11}+4004\alpha^2\\
&[\alpha(99\alpha+284)+288]y^9-3003\alpha\Big(\alpha[\alpha(557\alpha+2320)+4320]+2640\Big)y^7\\
&+14014\Big(\alpha\Big\{\alpha[\alpha(331\alpha+1832)+4800]+5760\Big\}+2880\Big)y^5-105105[\alpha(\alpha+4)\\
&+8][\alpha(83\alpha+240)+360]y^3\Bigg)+273K\Bigg[-256\Big\{\Big(\alpha\Big(\alpha[\alpha(131\alpha\\
&+1210)+5775]+13860\Big)+17325\Big\}+63\alpha^4y^{11}-616\alpha^3(\alpha+2)y^9+165\alpha^2\Big[19\alpha\\
&(\alpha+4)+112\Big]y^7-9240\alpha(\alpha+2)[\alpha(\alpha+4)+8]y^5+17325[\alpha(\alpha+4)+8]^2y^3\Bigg]\Bigg)\\
&+7JKyR_e^2P_r^2\Bigg(9009\Big[\alpha\Big\{\alpha[\alpha(99\alpha+932)+4560]+11200\Big\}+14400\Big]+189\alpha^4y^{12}\\
&-2184\alpha^3(\alpha+2)y^{10}+715\alpha^2[19\alpha(\alpha+4)+112]y^8-51480\alpha(\alpha+2)[\alpha(\alpha+4)\\
&+8]y^6+135135[\alpha(\alpha+4)+8]^2y^4-4992\Big[\alpha\Big\{\alpha\big[\alpha(131\alpha+1210)+5775\big]\\
&+13860\Big\}+17325\Big]y\Bigg)+3632428800K(1-4R)^2\Bigg],
\end{aligned}
\tag{47}
$$

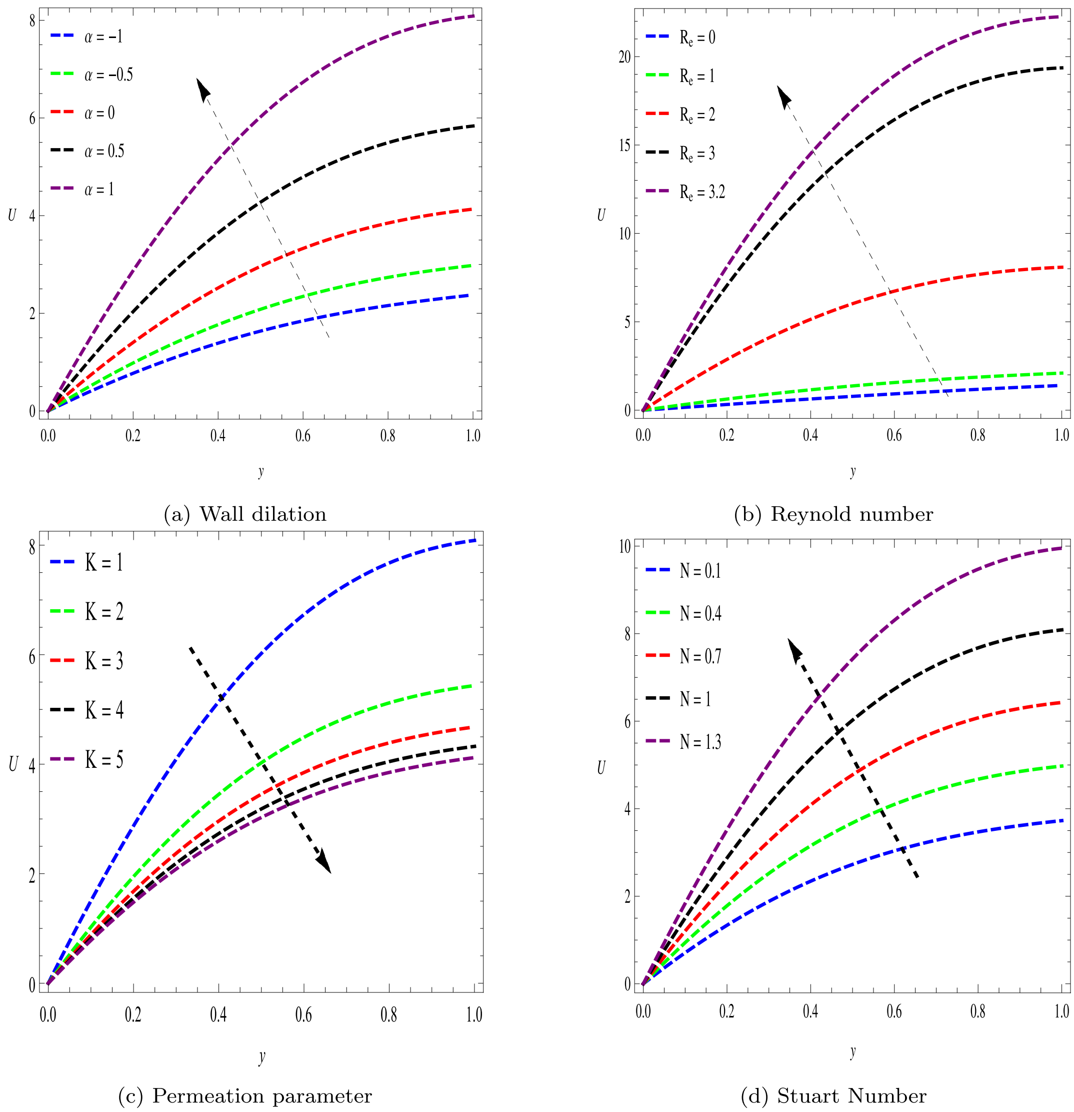

(a) Wall dilation (b) Reynold number

(c) Permeation parameter (d) Stuart Number

Fig. 3. Effects of parameters on axial velocity.

To solve for pressure gradient, by substituting Eq. (47) into Eq. (32) and integrating the resulting equation, between the bottom wall pressure $P = P_w = 1$ and the top wall pressure at $\frac{dP}{dy} = 0$, yields pressure variation as

$$
\begin{aligned}
&P(y)\\
&= \frac{1}{217945728000K(1-4R)^2}\\
&\times \Big[yG_r \Big(J(4R-1)yR_eP_r \Big\{ R_e \Big[K \Big\{ 4N \Big(134400(\alpha(\alpha(\alpha\\
&(957\alpha+7358)+29172)+55341)+54054)+4554\alpha^4y^{13}-105\alpha^3(671\alpha+964)y^{11}\\
&+5460\alpha^2[\alpha(99\alpha+284)+288]y^9-5005\alpha\big[\alpha\big(\alpha\{557\alpha+2320\}+4320\big)+2640\big]y^7\\
&+30030\big(\alpha\big[\alpha\{\alpha(331\alpha+1832)+4800\}+5760\big]+2880\big)y^5-315315\ [\ \alpha(\alpha+4)\\
&+8\ ]\ [\alpha(83\alpha+240)+360]y^3\ \Big)+105\ (\ 78\ \Big[\ \alpha\ \Big\{\ \alpha\big[\alpha(49285\alpha+443036)+2037420\big]\\
&+4693920\ \Big\}+5544000\ \Big]+990\alpha^4y^{12}-1512\alpha^4y^{11}-10374\alpha^3(\alpha+2)y^{10}\\
&+17472\alpha^3(\alpha+2)y^9+6006\alpha^2[9\alpha(\alpha+4)+52]y^8-5720\alpha^2[19\alpha(\alpha+4)\\
&+112]y^7-160875\alpha[\alpha+2][\alpha(\alpha+4)+8]y^6+411840\alpha[\alpha+2][\alpha(\alpha+4)+8]y^5\\
&+270270\big[\alpha(\alpha+4)+8\big]^2y^4-1081080\big[\alpha(\alpha+4)+8\big]^2y^3\ )\Big\}+4\ \Big(\ 134400\ \Big[\ \alpha\ \Big\{\ \alpha\\
&[\alpha(957\alpha+7358)+29172]+55341\ \Big\}+54054\ \Big]+4554\alpha^4y^{13}-105\alpha^3(671\alpha\\
&+964)y^{11}+5460\alpha^2\big[\alpha(99\alpha+284)+288\big]y^9-5005\alpha\ \Big(\ \alpha\big\{\alpha(557\alpha+2320)+4320\big\}\\
&+2640\ \Big)\ y^7+30030\big[\alpha\big(\alpha\big\{\alpha(331\alpha+1832)+4800\big\}+5760\big)+2880\big]y^5-315315\ [\ \alpha(\alpha\\
&+4)+8\ ]\ [\alpha(83\alpha+240)+360]y^3\ \Big)\Big]+420K\ (\ -4992\ \Big(\ \alpha\ \Big\{\ \alpha[\alpha(131\alpha+1210)+5775]\\
&+13860\ \Big\}+17325\ \Big)+189\alpha^4y^{11}-2184\alpha^3(\alpha+2)y^9+715\alpha^2[19\alpha(\alpha+4)+112]y^7\\
&-51480\alpha(\alpha+2)[\alpha(\alpha+4)+8]y^5+135135[\alpha(\alpha+4)+8]^2y^3\ )\Big\}+210JKyR_e^2P_r^2\\
&\Big[\ 9009\ \Big\{\ \alpha\big(\alpha\big[\alpha(99\alpha+932)+4560\big]+11200\big)+14400\ \Big\}+27\alpha^4y^{12}-364\alpha^3(\alpha\\
&+2)y^{10}+143\alpha^2[19\alpha(\alpha+4)+112]y^8-12870\alpha(\alpha+2)[\alpha(\alpha+4)+8]y^6\\
&+45045[\alpha(\alpha+4)+8]^2y^4-3328\ \Big(\ \alpha\ \Big\{\ \alpha\big[\alpha(131\alpha+1210)+5775\big]+13860\ \Big\}\\
&+17325\ \Big)\ y\ \Big]+217945728000K(1-4R)^2\ \Big)\\
&+217945728000(1-4R)^2(K+y)\ \Big].
\end{aligned}
\tag{48}
$$

As much as the perturbation method is valuable for analysing various flow dynamics involving small parameter variations, it can be computationally demanding to obtain more accurate results due to higher-order expansion. The technique is also sensitive to the choice of

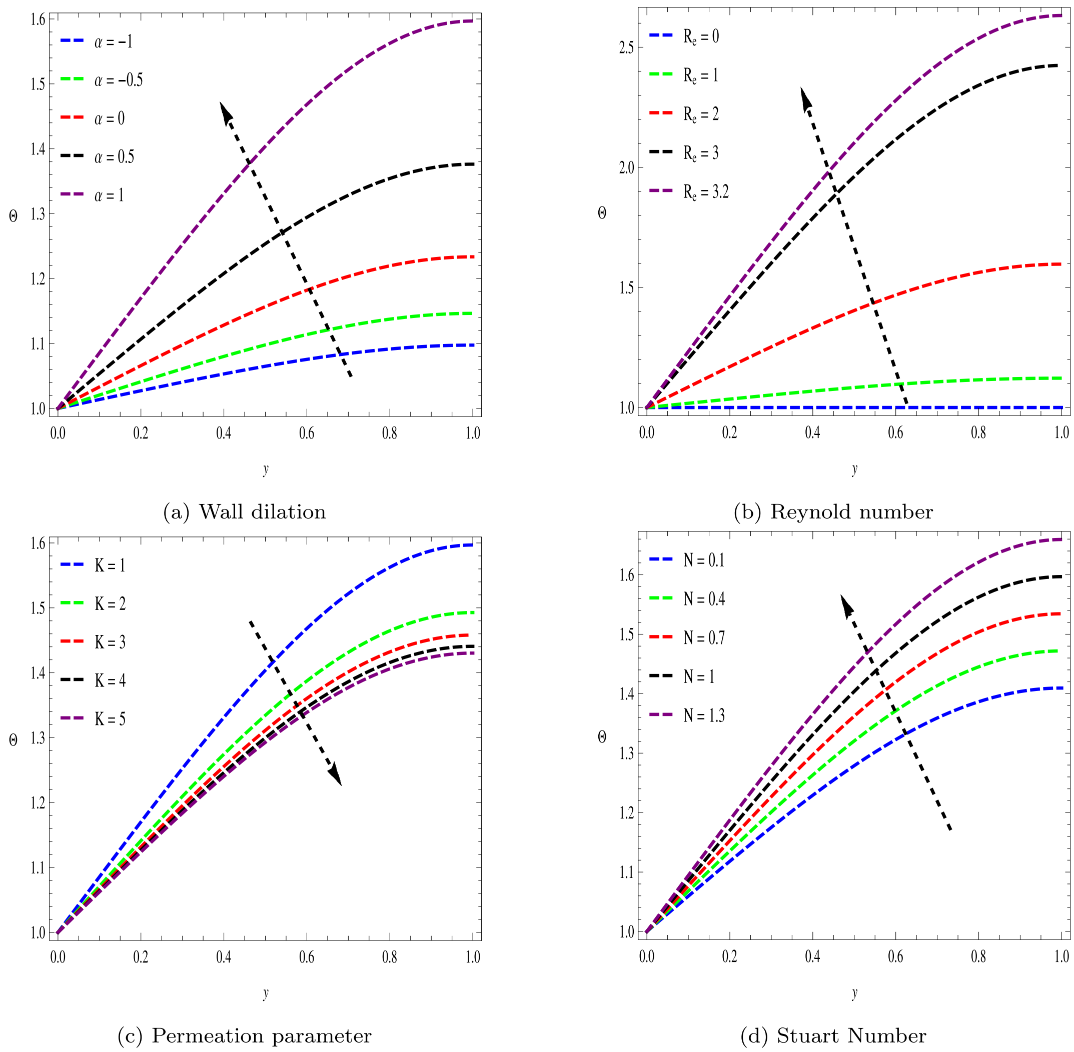

(a) Wall dilation

(b) Reynold number

(c) Permeation parameter

(d) Stuart Number

Fig. 4. Effects of parameters on internal temperature.

boundary condition; small changes in this condition can significantly affect the accuracy of the perturbation solution.

Because of the shear stress on the bottom wall caused by fluid motion, the skin friction coefficient is a parameter of physical significance since it shows how internal drag in a system behaves. Nusselt number physically illustrates the heat flux and radiation, which evaluate the quantity of heat exchange between the body and fluid at the boundary. Thus, these parameters of physical significance are defined as skin friction coefficient C_f and Nusselt number N_u below:

$$C_f = \frac{2\tau_w}{\rho {V_w}^2} \text{ and } N_u = \frac{\bar{x} q_w}{k(T_w - T_h)}, \tag{49}$$

where τ_w denotes the shear stress along the chamber's walls and q_w is the wall heat flux are defined as:

$$\tau_w = \mu \left(\frac{\partial \bar{u}}{\partial \bar{y}} \right)_{\bar{y}=0 \quad \bar{y}=1} \text{ and } q_w = -k \left(\frac{\partial T}{\partial \bar{y}} + \frac{16\sigma_r {T_w}^3 \partial T}{3k_r k \partial \bar{y}} \right)_{\bar{y}=0 \quad \bar{y}=1}, \tag{50}$$

Skin friction and Nusselt number occur at the chamber's top and bottom when $y = 1$ and $y = 0$, respectively. According to the current filter design, the above physical quantities take the following dimensionless form:

$$C_f = \frac{2}{R_e} \left(\frac{\partial u}{\partial y} \right)_{y=0\,,\, y=1} \text{ and } N_u = x \left(1 + 4R \right) \left(\frac{\partial \Theta}{\partial y} \right)_{y=0\,,\, y=1}. \tag{51}$$

The above dimensionless quantities will be used to analyse skin friction coefficient and heat flux during the filtration process in the next section.

4. Comparisons of solutions

In this section, we graphically compare the semi-analytical solutions obtained in the previous section with numerical solutions obtained using the mathematica package built-in function NDSolve.

According to Fig. 2 there is a correlation between the velocity, temperature, and pressure dynamics. The deviation noticed between the semi-analytical and numerical solutions for temperature, and pressure is caused by truncation error resulting from semi-analytical. Both solutions approximate similar profiles, which agree with the physics of the case study. For one to minimise the error between the numerical and semi-analytical solutions of temperature and velocity, the following parameters play an important role;

- Radiation (R): from the temperature, an acceptable error is achieved when radiating parameter is small enough, which physically, according to the system, acts as an emission radiation parameter meaning the fluid emits the radiation in the form of temperature.

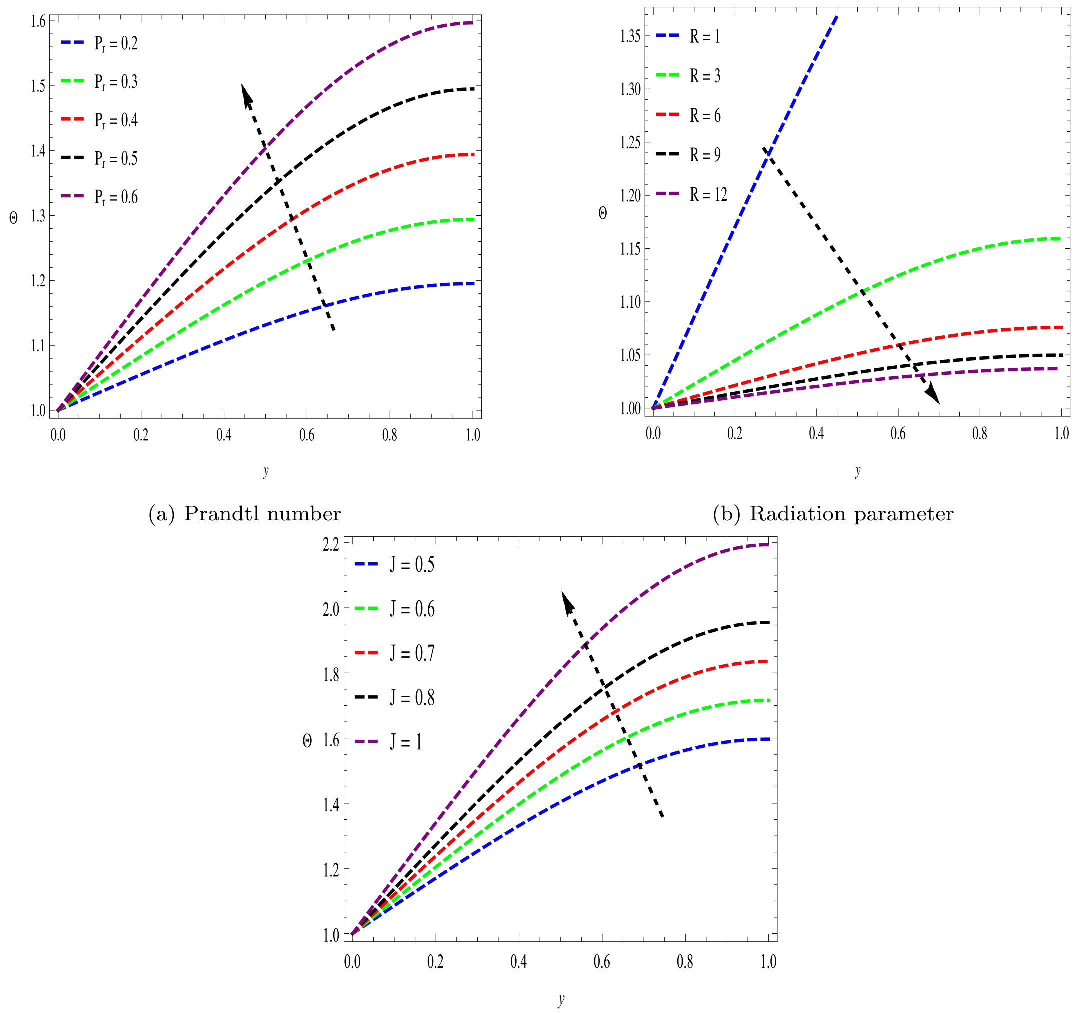

(a) Prandtl number

(b) Radiation parameter

(c) Joule heating parameter

Fig. 5. Effects of parameters on internal temperature.

- Permeation Reynolds number (R_e): for better or acceptable error, this parameter should also be small since higher values of R_e bring uncertainty in the output velocity. This is happening due to transition flow which is not allowed in this design since the flow is laminar; therefore, R_e should be between $0 \leq R_e \leq 1$.

When these two parameters are kept lower, the error in the solutions is also minimal. The numerical outcomes of the axial fluid velocity are validated by comparing the current flow results at different channel positions with those of Jafaryar et al.[44] The Table 1 shows that the results of the current study are accurate to order 2 with those of[44] solved by the optimal homotopy asymptotic method.

Table 1
Numerical outcomes of outflow velocity for $N = G_r = G_c = P_r = J = R = 0$ and $K \longrightarrow \infty$ compared with OHAM.

	$\alpha = 0,\ Re = 1$	
y	Present	OHAM[44]
0.0	0	0
0.1	0.17421	0.17176
0.2	0.33539	0.337421
0.3	0.49838	0.491359
0.4	0.62953	0.628838
0.5	0.74937	0.746307
0.6	0.84699	0.841553
0.7	0.91240	0.91371
0.8	0.96911	0.963137
0.9	0.98356	0.991199
1	0.99992	1

5. Results and discussion

This section depicts the impact of the relevant parameters on the velocity, temperature, and pressure of a steady, incompressible fluid inside the filter channel. How the pertinent parameters lead to optimal permeate outflow and temperature distribution, have been analysed in detail. Imperative graphs are enlisted to enrich the section. The drag coefficient and local heat transfer are also discussed in depth. For simulation, the parametric inputs are considered as

$$\alpha = 1, \quad P_r = 0.6, \quad K = 1, \quad G_r = 1, \quad N = 1, \quad R_e = 2, \quad R = 1, \quad J = 0.5,$$

According to the filter design, the ranges of physical parameters are such that the permeation Reynolds number ranges between $0 \leq R_e \leq 3.2$ to maintain laminar flow through a porous medium. The values $-1 \leq \alpha \leq 1$ are picked to study how flow properties are affected by the filter chamber volume. $\alpha > 0$ represents expansion, while $\alpha < 0$ show contraction. The Prandtl number range P_r is chosen to examine how momentum diffusivity ($P_r < 1$) and thermal diffusivity ($P_r > 1$) dominance behaves inside the filter chamber. For analysis, $P_r < 1$ is picked to maximise the permeates outflow. For the effectiveness of the

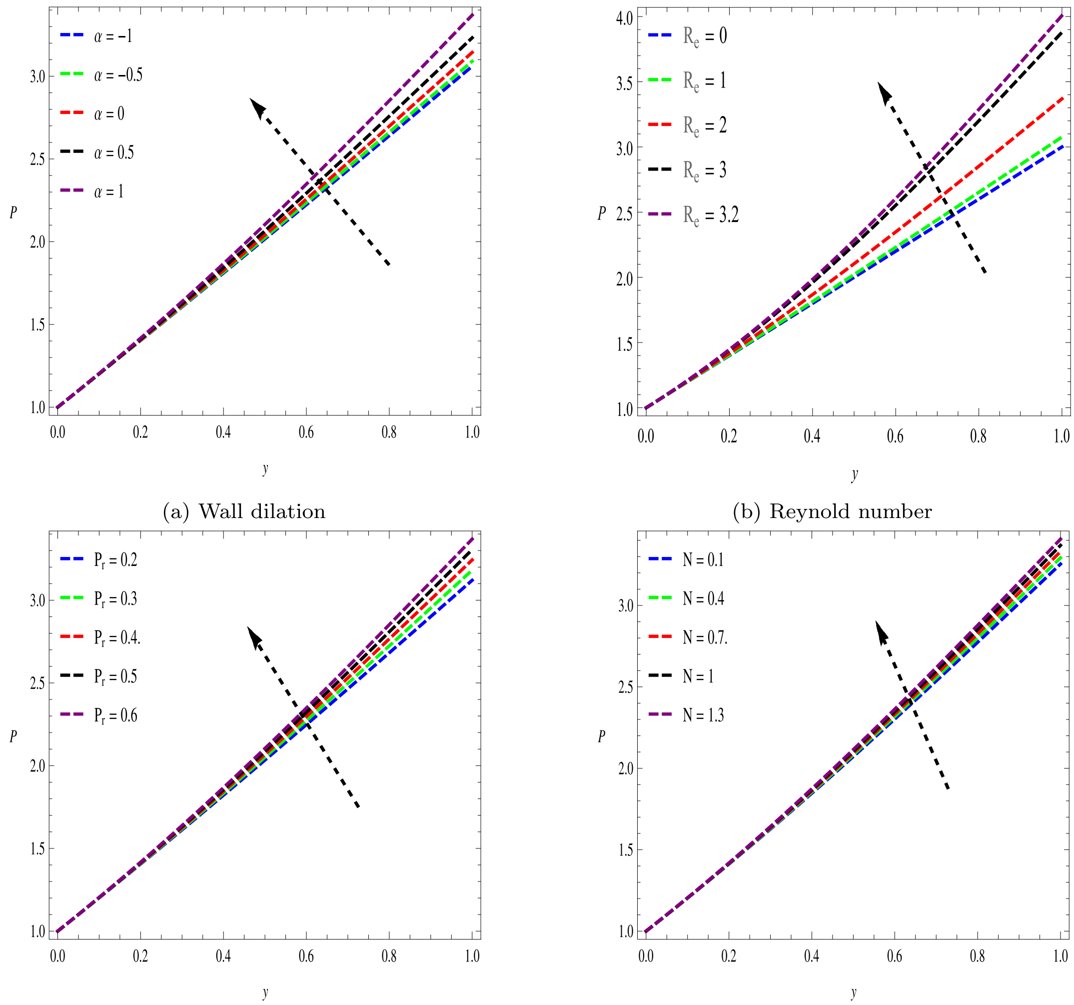

(a) Wall dilation (b) Reynold number (c) Prandtl number (d) Stuart Number

Fig. 6. Effects of parameters on internal pressure variation.

permeability, $1 \leq K \leq 5$ is picked since smaller values of K indicate big pores and bigger values of small pores of the medium. The values $N \geq 0$ effectively restrict the magnetic reactive impurities from entering the filter chamber while minimising reverse flow. The values $R \geq 0$ were preferred to investigate how emission ($R > 0$) influences fluid flow properties. Since high resistance (electrically conducting fluid acting as a resistor) produces more heat, the Joule/resistive heating parameter was chosen as $J \geq 0$.

5.1. The effects of various parameters on the axial velocity

Fig. 3 represents how the changes in the axial velocity profiles are affected by parameters such as α, R_e, K and N during the stable filtration.

Fig. 3(a) outlines the axial velocity changes due to the chamber wall dilation rate. Expanding the filter chamber ($\alpha > 0$) while injecting the fluid increases the axial fluid velocity. This is because the mass flow rate increases when expanding and injecting to preserve mass conservation.. It can be observed that the axial fluid velocity diminishes when the filter chamber space is reduced ($\alpha < 0$) due to the difficulty of fluid particle movement within a small area. In Fig. 3(b), the axial velocity enhances for $R_e > 0$. The effects seem minor near the bottom wall due to the no-slip condition, but near the upper wall, variation is noticed due to the impact of fluid injection and moving wall. The fluid injection inside the chamber increases momentum, increasing axial velocity. Fig. 3(c) portrays the reduction of axial fluid velocity inside the filtering chamber as the pore sizes become large. Bigger pore sizes cause a delay in fluid movement in the axial direction as particles move towards the pore surfaces. Fig. 3(d) addresses the impression of the magnetic force (N) on the axial fluid velocity. It is observed that stronger magnetic force gives rise to axial velocity. The increase in axial velocity is due to the binding effects that arise when a magnet pulls particles towards the upper moving wall such that the moving wall increases the movement of the internal flow.

5.2. Temperature distribution under the effects of various parameters

Figs. 4 and 5 display how different parameters affect the internal fluid temperature profiles during the stable filtration process.

The internal fluid temperature profiles in Figs. 4(a) and 4(b) increase when the chamber expands, and there is more fluid injection. This is due to increased internal fluid bulk, which improves heat absorption when the system introduces more particles that absorb temperature better than with few particles. Also, work done on the fluid during expansion increases the internal temperature. Enlarging the filter medium pore sizes (decrease in permeation) enhances the temperature profile, as shown in Fig. 4(c). The fluid outflow delay is experienced, leading to more temperature absorption than when filter medium pore sizes are small. Fig. 4(d) exhibits the magnetic force intensity on the internal fluid temperature profiles. The internal fluid

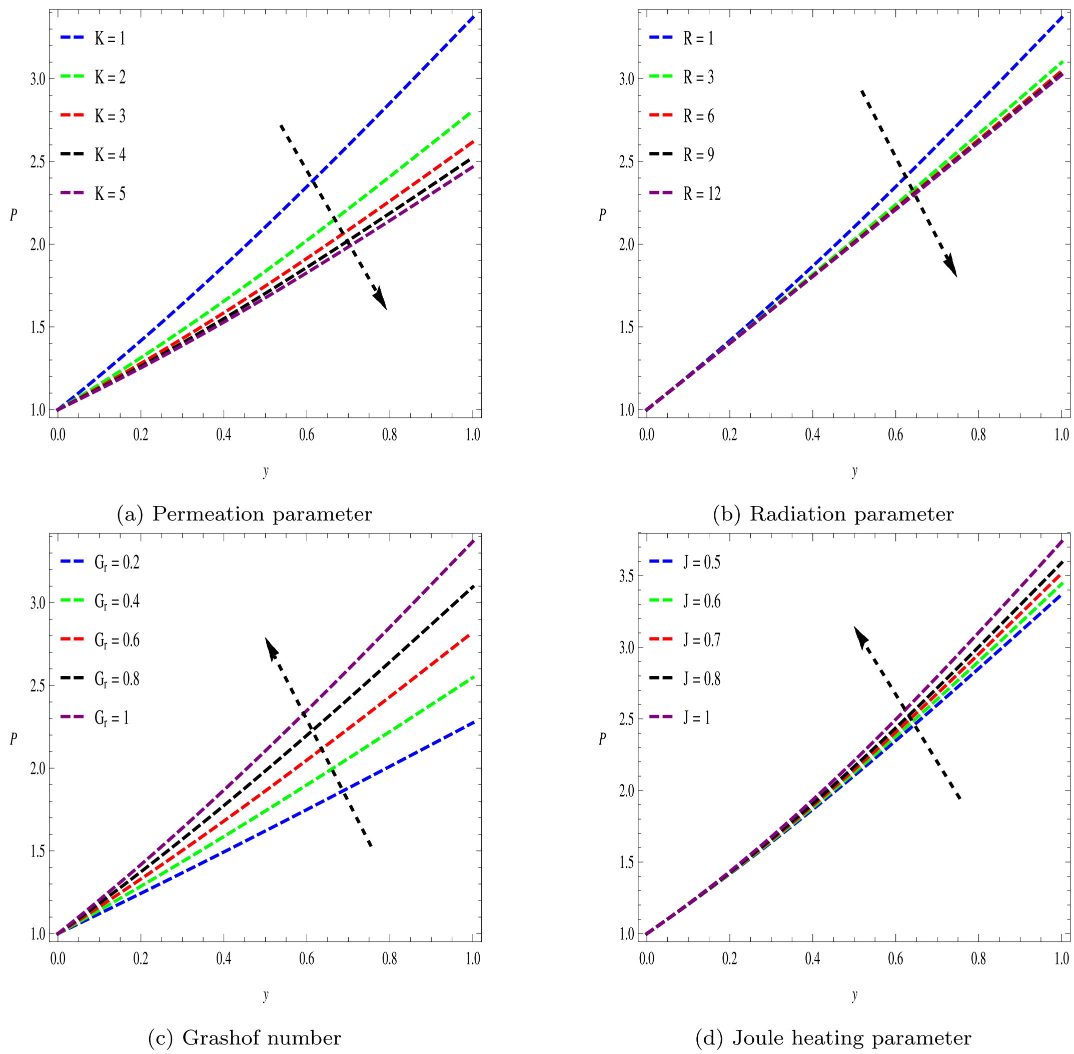

(a) Permeation parameter (b) Radiation parameter (c) Grashof number (d) Joule heating parameter

Fig. 7. Effects of parameters on internal pressure variation.

temperature is found to increase as the values of the magnetic force increase. Practically, higher magnetic force values bind particles such that they become heavier, increase contact with the heated wall, and absorb more heat; thus, internal temperature increases.

It is depicted in Fig. 5(a) that internal temperature profiles increases as the values of the Prandtl number increases. The internal fluid particles absorbs enough heat since the thermal diffusion dominates inside the filter chamber, leading to an increased internal temperature. Since the system emits energy in a form of radiation, thus, increasing R leads to an internal temperature drop, as shown in Fig. 5(b). The internal fluid temperature profiles rise, as shown in Fig. 5(c), for higher values of the Joule heating parameter as higher values of the Joule heating parameter increase heat resistance in the chamber, leading to a increase in temperature.

5.3. Pressure distribution under the effects of various parameters

Fig. 6 depicts that the internal pressure increases when the chamber volume, injection, Prandtl number and Stuart number increase. This pressure increase results from the internal velocity and temperature increase when these parameters increase.

It can be noted that in Fig. 7(a), the increase in permeation parameter decreases internal pressure whereas, the increase in radiation, Grashof number and Joule heating increases pressure, as shown in Figs. 7(b)–7(d) respectively. These behaviours are due to the result of permeation leading to a decrease in the internal temperature as well as the increase in temperature due to the increase in Joule heating. The increase due to the density variation, which increases movement along the direction of gravity when the Grashof number increase, which leads to an increase in internal work done and pressure, as depicted in Fig. 7(c).

5.4. The skin friction effects of various parameters on the axial velocity

Fig. 8 illustrates the impact of parameters on the internal friction coefficient during steady-state operation.

Figs. 8(a) and 8(b) reveal that expansion and enhancement of injection amplify the drag coefficient. Injection and wall expansion increase the internal fluid bulk resulting in more friction coefficient caused by heavier fluid bulk moving at higher velocity. An increase in magnetic force leads to a swelling in the internal drag coefficient due clustering of particles generated by the strengthening magnetic force see Fig. 8(d). According to Fig. 8(c), the internal friction coefficient growth is caused by the difficulty of fluid particles moving through the smaller pore sizes leading to internal drag generation.

5.5. Effects of Nusselt number Nu on temperature

Figs. 9 and 10 illustrate how parameters affect the heat transferred between the filter walls and internal fluid during steady-state operation.

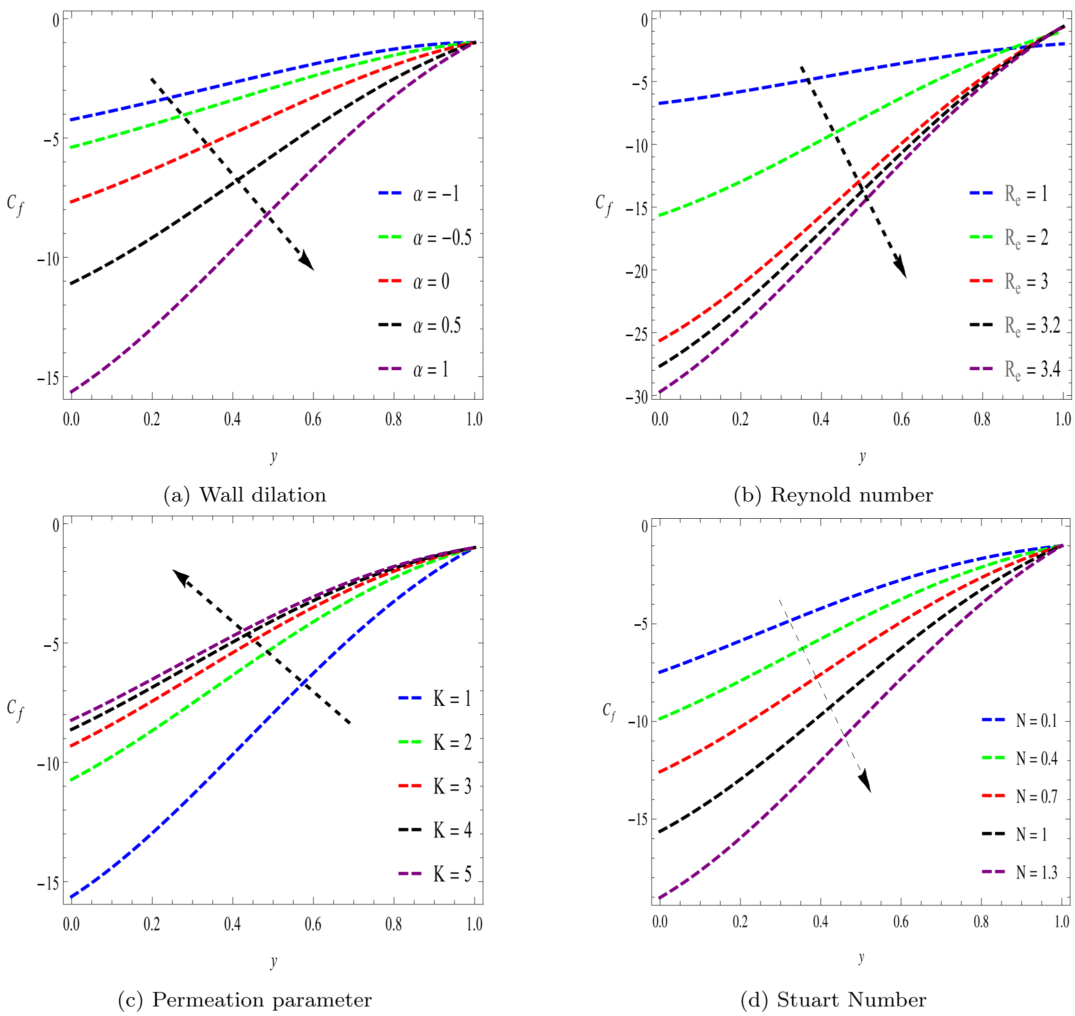

Fig. 8. Effects of parameters on friction coefficient.

From Figs. 9(a) and 9(b), it can be noted that the transfer of heat decreases when the filter chamber walls expand and as well as when the fluid injection rate increases. Heat transfer happens faster when the internal fluid bulk is more than when the internal fluid bulk is small since fewer particles reach internal thermal equilibrium faster than more fluid particles. Fig. 9(c) discloses that reducing the filter medium pore sizes (high permeation) enhances the heat transfer inside the filter chamber. Since small pore sizes decrease the internal fluid bulk due to the porous medium occupying the chamber space such that the system allows fewer internal particles, which enhances heat transfer. The increase in magnetic force, as shown in Fig. 9(d), decreases heat transfer since stronger magnetic force pulls particles away from the bottom wall and decreases contact between the top wall and the fluid bulk such that heat absorption of the bottom wall decrease.

Higher values of Prandtl number result in less internal thermal diffusion leading to a decrease in heat transfer, as shown in Fig. 10(a). According to Figs. 10(b) and 10(c), the system experiences more internal heat flux when fluid radiates more and when the Joules heating parameter is less. This heat flux is caused by high radiation heating up the fluid faster, such that the temperature gradient decreases. In contrast, less Joule heat leads to a higher internal temperature; thus, heat transfer from the wall becomes less.

6. Concluding remarks

The flow and heat distribution in an horizontal filter channel during filtration were investigated using Lie symmetry analysis and the double perturbation method. The wall dilation (α), Reynolds number (Re), Grashof number (Gr), Prandtl number (Pr), Radiation number (R), and Joule heating parameter (J) are critical characteristics that affect the internal flow and heat distribution during the filtering process which were analysed to find optimum permeates outflow. Additionally, the problem's mathematical representation follows the fundamental conservation laws for mass, momentum, and energy, respectively. According to the study's conclusions, the following dynamics are essential to maximise permeates production during the filtration process.

(1) **Internal velocity:** To increase outflow velocity, more wall dilation, injection, magnetic force, and small pore size are required throughout. The movement of the top wall while injecting fluid also increases the internal velocity.
(2) **Internal temperature:** When the permeates outflow increases, the internal temperature increases since the internal temperature enhances the internal work done such that the system outflow increases.

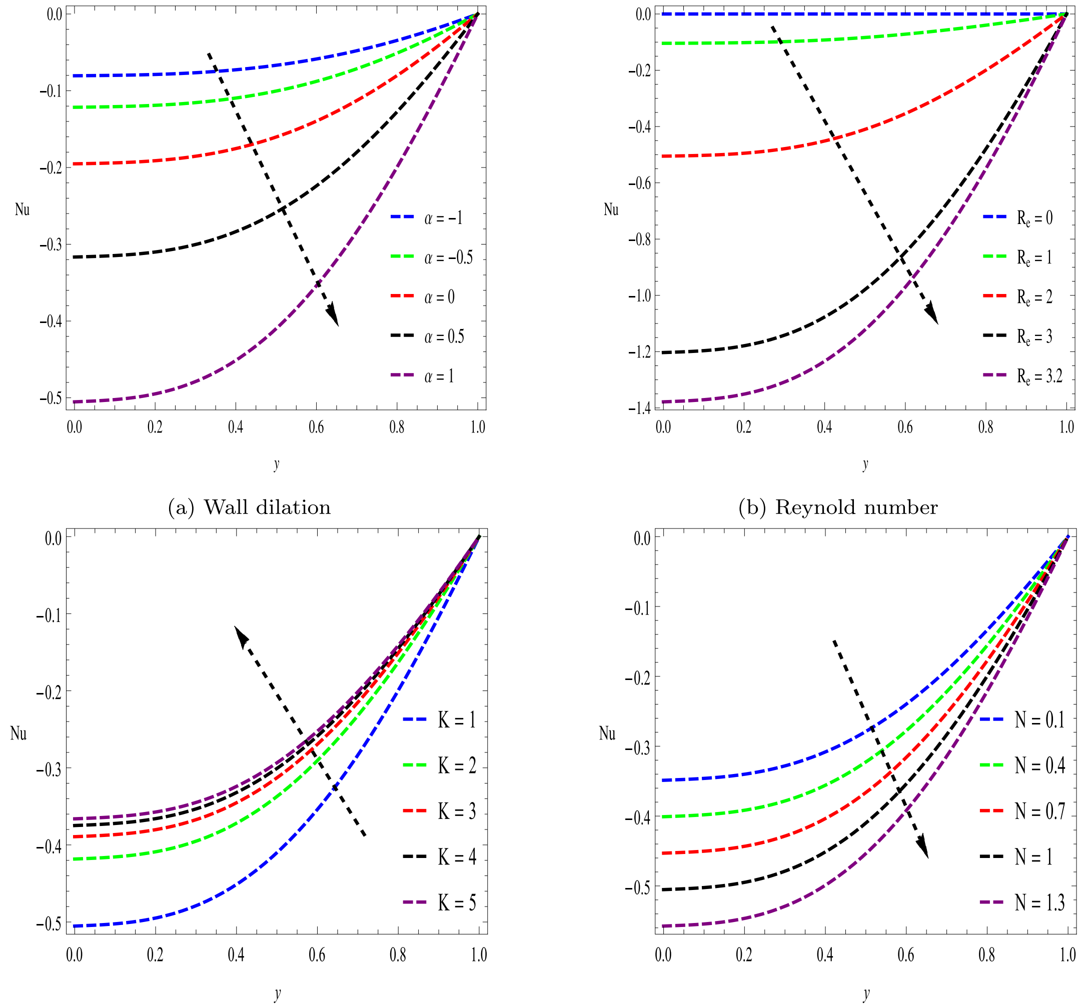

(a) Wall dilation (b) Reynold number (c) Permeation parameter (d) Stuart Number

Fig. 9. Effects of parameters on Nusselt number.

(3) **Internal pressure:** Throughout the operation, the internal pressure increases when the internal work done increases. Since the system is pressure driven, thus the increase in pressure drives permeates out of the chamber.
(4) **Friction coefficient:** More chamber volume, fluid injection and Stuart number, as well as small pores size, are needed to minimise internal friction during operation.
(5) **Nusselt number:** To increase heat flux during operation, less chamber volume, fluid injection, magnetic force, Prandtl number, and Joule heating are required.

To understand the dynamic filtration process better, one can study the transition from the steady state regime to the unsteady state regime and study the dynamics of the filtration process in three dimensions by including the analysis of momentum variation in the z-direction. Also, the effects of density variation can be investigated.

Funding

The authors affirm that they have no known financial or interpersonal conflicts that would have appeared to have an impact on the research presented in this manuscript.

CRediT authorship contribution statement

Thabo Joseph Itumeleng: Conceptualisation, Model formulation, Visualisation, Analysis, Discussion, Writing – editing. **Gabriel Magalakwe:** Conceptualisation, Model formulation, Analytical computation, Analysis, Supervision, Reviewing. **Modisawatsona Lucas Lekoko:** Model formulation, Analytical computation, Software Writing – editing. **Letlhogonolo Daddy Moleleki:** Supervision, Analytical computation, Software, Writing – editing.

Declaration of competing interest

The authors declare that they have no known competing financial interests or personal relationships that could have appeared to influence the work reported in this paper.

Data availability

No data was used for the research described in the article.

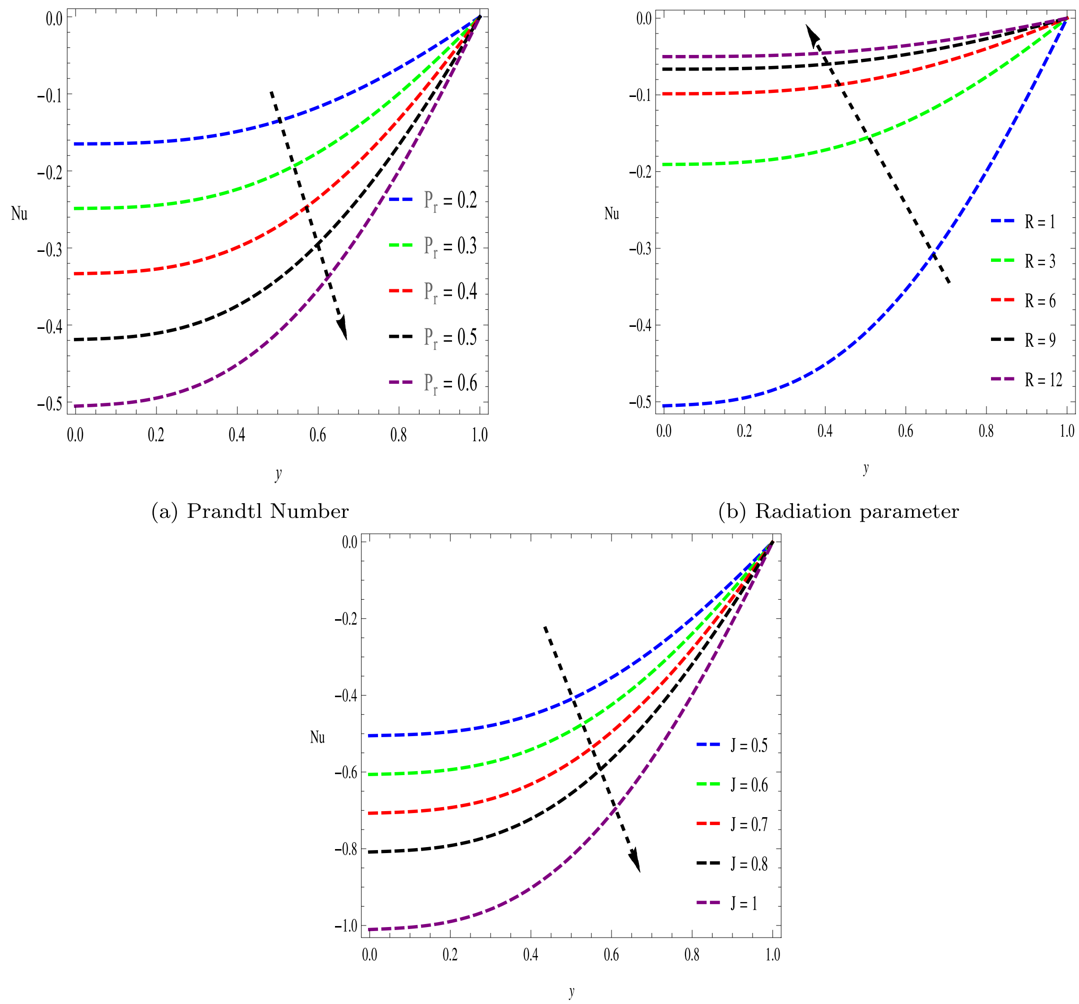

(a) Prandtl Number (b) Radiation parameter

(c) Joule heating parameter

Fig. 10. Effects of parameters on Nusselt number.

Appendix. Appendix section

$$A_1 = KN + K + 1,\ A_2 = KN + 1,$$

$$A_3 = -21\left[K\left(K\left[N\left(43N + 110\right) + 60\right] + 86N + 110\right) + 43\right],$$

$$A_4 = 35\left[K\left(13N + 28\right) + 13\right],\ A_5 = K\left[K\left(N(5N + 8) - 12\right) + 10N + 8\right] + 5,$$

$$A_6 = K(5N + 6) + 5,\ A_7 = K\left[K\left(N\left(25N + 48\right) - 18\right) + 50N + 48\right] + 25,$$

$$A_8 = K\left[K\left(2N(53N + 105) + 45\right) + 212N + 210\right] + 106,$$

$$A_9 = K\left[K\left(N(16N + 23) - 45\right) + 32N + 23\right] + 16,$$

$$A_{10} = K\left(83N + 90\right) + 83,\ A_{11} = K\left(2N + 3\right) + 2,$$

$$A_{12} = 9K\left[K\left(N(1623N + 3296) + 1260\right) + 3246N + 3296\right],$$

$$A_{13} = 20K\left(2N + 3\right) + 40,\ A_{14} = K\left(7N + 6\right) + 7,\ A_{15} = K\left(11N + 12\right) + 11.$$

References

1. Jackson J. A study of squeezing flow. *Appl Sci Res, Sect A*. 1963;11:148–152.
2. Siddiqui AM, Irum S, Ansari AR. Unsteady squeezing flow of a viscous MHD fluid between parallel plates, a solution using the homotopy perturbation method. *Math Model Anal*. 2008;13(4):565–576.
3. Domairry G, Aziz A. Approximate analysis of MHD squeeze flow between two parallel disks with suction or injection by homotopy perturbation method. *Math Probl Eng*. 2009;2009.
4. Rashidi MM, Shahmohamadi H, Dinarvand S. Analytic approximate solutions for unsteady two-dimensional and axisymmetric squeezing flows between parallel plates. *Math Probl Eng*. 2008;2008.
5. Grimm R. Squeezing flows of Newtonian liquid films an analysis including fluid inertia. *Appl Sci Res*. 1976;32:149–166.
6. Prasad D, Singh P, Sinha P. Thermal and squeezing effects in non-Newtonian fluid film lubrication of rollers. *Wear*. 1987;119(2):175–190.
7. Rodin GJ. Squeeze film between two spheres in a power-law fluid. *J Non-Newton Fluid Mech*. 1996;63(2–3):141–152.
8. Lian G, Xu Y, Huang W, Adams MJ. On the squeeze flow of a power-law fluid between rigid spheres. *J Non-Newton Fluid Mech*. 2001;100(1–3):151–164.
9. Sweet E, Vajravelu K, Van Gorder RA, Pop I. Analytical solution for the unsteady MHD flow of a viscous fluid between moving parallel plates. *Commun Nonlinear Sci Numer Simul*. 2011;16(1):266–273.
10. Hayat T, Nawaz M, Hendi AA, Asghar S. MHD squeezing flow of a micropolar fluid between parallel disks. *J Fluids Eng*. 2011;133(11).
11. Mustafa M, Hayat T, Obaidat S. On heat and mass transfer in the unsteady squeezing flow between parallel plates. *Meccanica*. 2012;47:1581–1589.
12. Hayat T, Yousaf A, Mustafa M, Asghar S. Influence of heat transfer in the squeezing flow between parallel disks. *Chem Eng Commun*. 2012;199(8):1044–1062.
13. Lahmar S, Kezzar M, Eid MR, Sari MR. Heat transfer of squeezing unsteady nanofluid flow under the effects of an inclined magnetic field and variable thermal conductivity. *Phys A*. 2020;540:123138.

14. Khan MS, Shah RA, Khan A. Effect of variable magnetic field on the flow between two squeezing plates. *Eur Phys J Plus*. 2019;134(5):219.
15. Hayat T, Muhammad T, Qayyum A, Alsaedi A, Mustafa M. On squeezing flow of nanofluid in the presence of magnetic field effects. *J Mol Liq*. 2016;213:179–185.
16. Salehi S, Nori A, Hosseinzadeh K, Ganji D. Hydrothermal analysis of MHD squeezing mixture fluid suspended by hybrid nanoparticles between two parallel plates. *Case Stud Therm Eng*. 2020;21:100650.
17. Rahimi-Gorji M, Pourmehran O, Gorji-Bandpy M, Ganji D. Unsteady squeezing nanofluid simulation and investigation of its effect on important heat transfer parameters in presence of magnetic field. *J Taiwan Inst Chem Eng*. 2016;67:467–475.
18. Abbas N, Rehman KU, Shatanawi W, Malik M. Numerical study of heat transfer in hybrid nanofluid flow over permeable nonlinear stretching curved surface with thermal slip. *Int Commun Heat Mass Transfer*. 2022;135:106107,
19. Gumber P, Yaseen M, Rawat SK, Kumar M. Heat transfer in micropolar hybrid nanofluid flow past a vertical plate in the presence of thermal radiation and suction/injection effects. *Partial Differ Equ Appl Math*. 2022;5:100240.
20. Flow and heat transfer of nanofluid with injection through an expanding or contracting porous channel under magnetic force field. *Eng Sci Technol, Int J*. 2018;21(3):486–494.
21. Akinshilo AT. Thermal performance evaluation of MHD nanofluid transport through a rotating system undergoing uniform injection/suction with heat generation. *BioNanoScience*. 2019;9(3):740–748.
22. Akinshilo AT. Steady flow and heat transfer analysis of third-grade fluid with porous medium and heat generation. *Eng Sci Technol, Int J*. 2017;20(6):1602–1609.
23. Rasheed HU, Zeeshan, Islam S, Ali B, Shah Q, Ali R. Implementation of shooting technique for Buongiorno nanofluid model driven by a continuous permeable surface. *Heat Transfer*. 52(4):3119–3134.
24. Ur Rasheed H, AL-Zubaidi A, Islam S, Saleem S, Khan Z, Khan W. Effects of Joule heating and viscous dissipation on magnetohydrodynamic boundary layer flow of Jeffrey nanofluid over a vertically stretching cylinder. *Coatings*. 2021;11(3).
25. Rasheed HU, Islam SZ, Abbas T, Khan J. Analytical treatment of MHD flow and chemically reactive Casson fluid with Joule heating and variable viscosity effect. *Waves Random Complex Media*. 2022:1–17.
26. Abel MS, Datti P, Mahesha N. Flow and heat transfer in a power-law fluid over a stretching sheet with variable thermal conductivity and non-uniform heat source. *Int J Heat Mass Transfer*. 2009;52(11–12):2902–2913.
27. Patel M, Timol M. Numerical treatment of Powell–Eyring fluid flow using method of satisfaction of asymptotic boundary conditions (MSABC). *Appl Numer Math*. 2009;59(10):2584–2592.
28. Andersson H, Bech K, Dandapat B. Magnetohydrodynamic flow of a power-law fluid over a stretching sheet. *Int J Non-Linear Mech*. 1992;27(6):929–936.
29. Sahoo B. Hiemenz flow and heat transfer of a third grade fluid. *Commun Nonlinear Sci Numer Simul*. 2009;14(3):811–826.
30. Olajuwon B. Convection heat and mass transfer in a hydromagnetic flow of a second grade fluid in the presence of thermal radiation and thermal diffusion. *Int Commun Heat Mass Transfer*. 2011;38(3):377–382.
31. Magalakwe G, Lekoko M, Modise K, Khalique CM. Lie group analysis for MHD squeezing flow of viscous fluid saturated in porous media. *Alex Eng J*. 2019;58(3):1001–1010.
32. Bluman GW, Kumei S. *Symmetries and Differential Equations, Vol. 81*. Springer Science & Business Media; 2013.
33. Pal D, Roy N. Lie group transformation on MHD double-diffusion convection of a Casson nanofluid over a vertical stretching/shrinking surface with thermal radiation and chemical reaction. *Int J Appl Comput Math*. 2018;4:1–23.
34. Agrawal P, Dadheech PK, Jat R, Bohra M, Nisar KS, Khan I. Lie similarity analysis of MHD flow past a stretching surface embedded in porous medium along with imposed heat source/sink and variable viscosity. *J Mater Res Technol*. 2020;9(5):10045–10053.
35. Abdel-Wahed M, Akl M. Effect of hall current on MHD flow of a nanofluid with variable properties due to a rotating disk with viscous dissipation and nonlinear thermal radiation. *AIP Adv*. 2016;6(9):095308.
36. Shah Z, Dawar A, Kumam P, Khan W, Islam S. Impact of nonlinear thermal radiation on MHD nanofluid thin film flow over a horizontally rotating disk. *Appl Sci*. 2019;9(8):1533.
37. Bluman GW, Cheviakov AF, Anco SC. *Applications of Symmetry Methods to Partial Differential Equations, Vol. 168*. Springer; 2010.
38. Ibragimov NH, Ibragimov NK. *Elementary Lie Group Analysis and Ordinary Differential Equations, Vol. 197*. Wiley New York; 1999.
39. Magalakwe G, Lekoko M, Modise K, Khalique CM. Lie group method solution for two-dimensional heat and viscous flow driven by injection through a deformable rectangular channel with porous walls. *Math Model Optim Eng Probl*. 2020:89–114.
40. Ibragimov NH. *Practical Course in Differential Equations and Mathematical Modelling, A: Classical and New Methods. Nonlinear Mathematical Models. Symmetry and Invariance Principles*. World Scientific Publishing Company; 2009.
41. Van Dyke M. Perturbation methods in fluid mechanics/annotated edition. *NASA STI/Recon Tech Rep A*. 1975;75:46926.
42. Aziz A, Na TY. *Perturbation Methods in Heat Transfer*. Washington, 1984.
43. Holmes MH. *Introduction to Perturbation Methods, Vol. 20*. Springer Science & Business Media; 2012.
44. Jafaryar M, Farkhadnia F, Mohammadian E, Hosseini M, Khazaee A. Analytical investigation of laminar flow through expanding or contracting gaps with porous walls. *Propuls Power Res*. 2014;3(4):222–229.